

Article

Effect of the Alkaline Metal Ion on the Crystal Structure and Magnetic Properties of Heterometallic Gd^{III}-V^{IV} Complexes Based on Cyclobutane-1,1-Dicarboxylate Anions

Evgeniya S. Bazhina ^{1,*}, Alexander A. Korlyukov ², Julia K. Voronina ¹, Konstantin A. Babeshkin ¹, Elena A. Ugolkova ¹, Nikolay N. Efimov ¹, Matvey V. Fedin ³, Mikhail A. Kiskin ^{1,*} and Igor L. Eremenko ^{1,2}

¹ N.S. Kurnakov Institute of General and Inorganic Chemistry of the Russian Academy of Sciences, Leninskiy Prosp. 31, 119991 Moscow, Russia; juliavoronina@mail.ru (J.K.V.); bkonstantan@yandex.ru (K.A.B.); tipperiri@yandex.ru (E.A.U.); nnefimov@yandex.ru (N.N.E.); ilerem@igic.ras.ru (I.L.E.)

² A.N. Nesmeyanov Institute of Organoelement Compounds of the Russian Academy of Sciences, Vavilova Str. 28, 119991 Moscow, Russia; alex@xrlab.ineos.ac.ru

³ International Tomography Center of the Siberian Branch of the Russian Academy of Sciences, Institutskaya Str. 3a, 630090 Novosibirsk, Russia; mfeidin@tomo.nsc.ru

* Correspondence: evgenia-vo@mail.ru (E.S.B.); mkiskin@igic.ras.ru (M.A.K.)



Citation: Bazhina, E.S.; Korlyukov, A.A.; Voronina, J.K.; Babeshkin, K.A.; Ugolkova, E.A.; Efimov, N.N.; Fedin, M.V.; Kiskin, M.A.; Eremenko, I.L. Effect of the Alkaline Metal Ion on the Crystal Structure and Magnetic Properties of Heterometallic Gd^{III}-V^{IV} Complexes Based on Cyclobutane-1,1-Dicarboxylate Anions. *Magnetochemistry* **2021**, *7*, 82. <https://doi.org/10.3390/magnetochemistry7060082>

Academic Editor: Marius Andruh

Received: 1 April 2021

Accepted: 29 May 2021

Published: 3 June 2021

Publisher's Note: MDPI stays neutral with regard to jurisdictional claims in published maps and institutional affiliations.



Copyright: © 2021 by the authors. Licensee MDPI, Basel, Switzerland. This article is an open access article distributed under the terms and conditions of the Creative Commons Attribution (CC BY) license (<https://creativecommons.org/licenses/by/4.0/>).

Abstract: A series of heterometallic Gd^{III}-V^{IV} compounds were synthesized by the reaction of VOSO₄·3H₂O with cyclobutane-1,1-dicarboxylic acid salts M₂(cbdc) (M = Na, Rb, Cs). The new compounds were formed by [Gd(VO)₂(cbdc)₄(H₂O)₈][−] trinuclear anionic units that were similar in composition but differed in structure, depending on the nature of the alkali metal cation incorporated in the crystal structure of the compound. In the case of Na⁺, the {GdV₂}[−] units were characterized by identical V···Gd distances and were linked into the 1D-polymeric chain [NaGd(VO)₂(cbdc)₄(H₂O)₁₀]_n (**1**). In the systems with Rb⁺ and Cs⁺, the V···Gd distances were different, and the {GdV₂}[−] units were linked into the 3D-framework {[RbGd(VO)₂(cbdc)₄(H₂O)₁₀]}_n·2.5H₂O (**2**) and the octanuclear molecule {[CsGd(VO)₂(cbdc)₄(H₂O)₁₁]}₂·5H₂O (**3**), respectively. According to *dc*-magnetic measurements, the V^{IV} and Gd^{III} ions were ferromagnetically coupled in compound **1** (*J*_{VGd} = 0.163 ± 0.008 cm^{−1}), while in compounds **2** and **3**, ferro- and weak antiferromagnetic exchange interactions were observed (*J*_{VGd} = 0.989 ± 0.028 and −0.089 ± 0.008 cm^{−1} for **2**, 0.656 ± 0.009 and −0.050 ± 0.004 cm^{−1} for **3**). Analysis of the EPR spectra of **1** revealed the presence of weak magnetic anisotropy of Gd^{III} ions (*D*~0.08 cm^{−1} and *E*/*D*~0.1–0.15). *Ac*-susceptibility measurements showed an occurrence the field-induced slow relaxation of magnetization in **1–3**.

Keywords: Gd^{III}-V^{IV} compounds; cyclobutane-1,1-dicarboxylic acid; crystal structure; exchange interactions; slow magnetic relaxation; EPR spectroscopy

1. Introduction

The interest in the directed synthesis of heterometallic compounds where 3*d* and 4*f* metal ions are combined in a single molecule is caused by the wide range of physicochemical properties they exhibit, including luminescent properties [1,2], molecular magnetism [3,4], magnetocaloric effect [5–9], and catalytic activity [10–12]. In addition, studies on such heterometallic compounds are of fundamental concern in order to elucidate the exchange interactions between paramagnetic centers of different nature, 3*d* and 4*f* metal ions, and the effect of these interactions on the dynamic characteristics of a single-molecule magnet (SMM), for example, the magnitude of the energy barrier to magnetization reversal Δ_{eff}. From this point of view, the most convenient objects for studies by physicochemical methods include systems with a 3*d* center containing one unpaired electron (*S* = 1/2, quantum spin), namely a Cu^{II} (3*d*⁹) or V^{IV} (3*d*¹) ion. To date, a number of Cu^{II}-4*f* systems, from molecular complexes to coordination polymers, have already been well

studied [8,13–18]. It has been shown that this class of compounds can be promising as magnetic coolers [4,19–22], and ferromagnetic interactions are often the prevailing type of spin-spin interactions in them [23–26]. Much less attention was paid to the synthesis of $V^{IV}-4f$ compounds and only a few studies on their magnetic behavior are known [27–35].

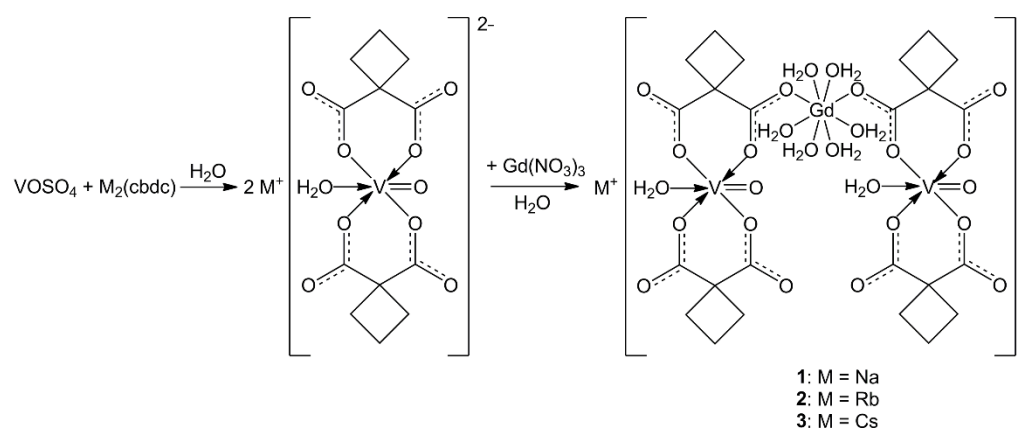
As it is known, the Gd^{III} ion lacks intrinsic magnetic anisotropy, which is observed in Dy^{III} , Tb^{III} , and other heavy 4f-ions. Because of this, the Gd^{III} ion by itself is ineffective in the design of SMM or single-ion magnets (SIM). Nevertheless, there are examples of Gd^{III} complexes exhibiting slow magnetic relaxation, which is due to the phonon bottleneck effect [36–44] or by the presence of weak anisotropy caused by orbital nondegeneracy of the ground state 8S [44].

We previously synthesized and characterized a series of heterometallic $Ln^{III}-V^{IV}$ compounds based on cyclobutane-1,1-dicarboxylate anions, in which three structural types were identified, depending on the nature (ionic radius) of Ln^{III} [45]. A further study of this system showed that the nature of the alkali metal introduced into the reaction as a salt of a dicarboxylic acid also affected the structure of the compound formed. This work aimed at varying the alkali metal cation M^I ($M^I = Na, Rb, Cs$) in the $M^I-Gd^{III}-V^{IV}$ system and studying its effect on the composition, structure, and magnetic properties of the resulting compounds.

2. Results and Discussion

2.1. Synthesis

The reaction of $VOSO_4 \cdot 3H_2O$, $Na_2(cbdc)$, and $Gd(NO_3)_3 \cdot 6H_2O$ in a 1:2:1 ratio in water afforded crystals of the 1D-polymeric compound $[NaGd(VO)_2(cbdc)_4(H_2O)_{10}]_n$ (**1**). Replacement of sodium cyclobutane-1,1-dicarboxylate $Na_2(cbdc)$ with $Rb_2(cbdc)$ in a similar reaction gave the 3D-polymer $\{[RbGd(VO)_2(cbdc)_4(H_2O)_{10}] \cdot 2.5H_2O\}_n$ (**2**), while the reaction with $Cs_2(cbdc)$ resulted in the crystallization of the octanuclear complex $\{[CsGd(VO)_2(cbdc)_4(H_2O)_{11}] \cdot 5H_2O\}_2$ (**3**) (Scheme 1).



Scheme 1. Scheme illustrating the formation of compounds 1–3.

2.2. Crystal Structure Description

Compounds **1** and **2** crystallize in monoclinic space group $C2/c$. Compound **2** contained 2.5 solvate water molecules. Compound **3** crystallizes in triclinic space group $P\bar{1}$ with 5 solvate water molecules. The basic structural unit of all the three compounds is the $[Gd(VO)_2(cbdc)_4(H_2O)_8]^{2-}$ ($\{GdV_2\}^-$) anionic complex with a trinuclear metal core. In this unit, gadolinium is the central atom, while the vanadium atoms are terminal ones and belong to bis-chelate moieties $\{(VO)(cbdc)_2(H_2O)\}$ (see Scheme 1). In complex **1**, the vanadium atoms were crystallographically equivalent (Figure 1), while the terminal vanadium atoms, V1 and V2, in compounds **2** and **3** were nonequivalent (Figures 2 and 3). The coordination polyhedron of vanadium (VO_6) is a distorted octahedron formed by six O atoms. Four O atoms of two chelating $cbdc^{2-}$ anions lie in the equatorial plane of the polyhedron,

while the axial positions are occupied by O atoms of the vanadyl moiety {V=O} and the water molecule. The central gadolinium atom in $\{GdV_2\}^-$ was linked to two terminal vanadium atoms due to bridging coordination of two O atoms of $cbdc^{2-}$ anions in the $\{(VO)(cbdc)_2(H_2O)\}$ moieties (Tables 1 and S1–S3).

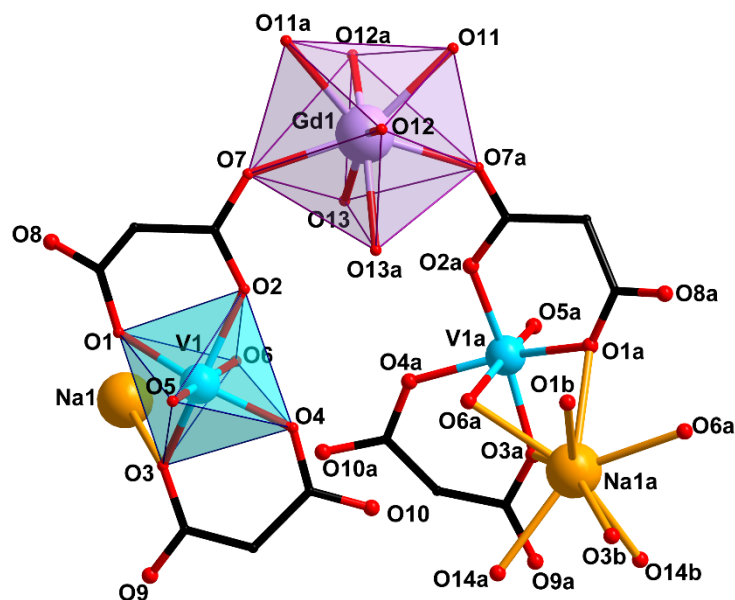


Figure 1. Structure of trinuclear unit $\{GdV_2\}^-$ and Na atom environment in compound 1 (H atoms and cyclic fragments of the carboxylate ligands are not shown). [Symmetry codes: (a) $1 - x, y, 0.5 - z$; (b) $1 + x, y, z$].

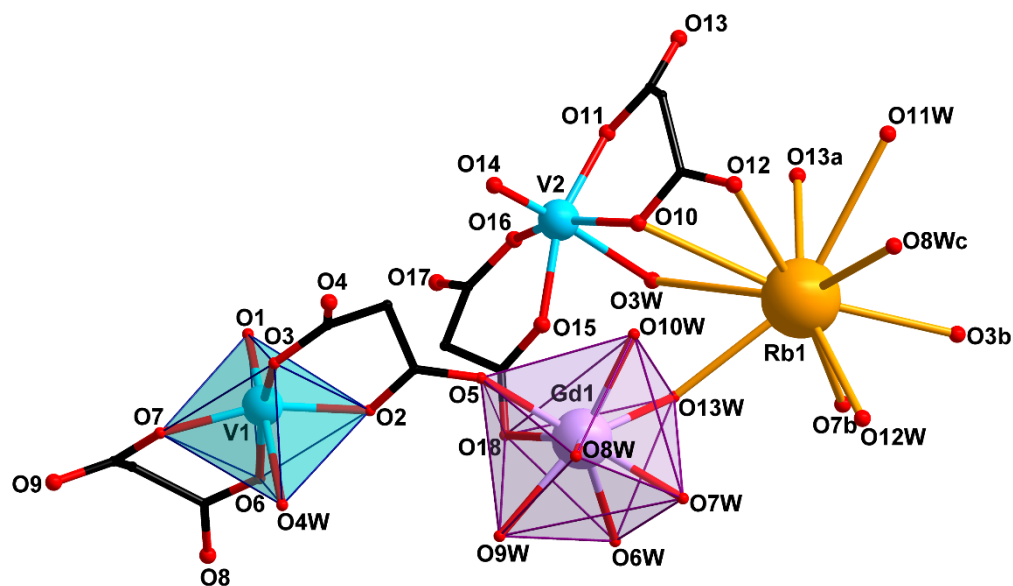


Figure 2. Structure of trinuclear unit $\{GdV_2\}^-$ and Rb atom environment in compound 2 (H atoms and cyclic fragments of the carboxylate ligands are not shown). [Symmetry codes: (a) $1 - x, y, 1.5 - z$; (b) $-0.5 + x, 0.5 + y, z$; (c) $1 - x, 2 - y, 1 - z$].

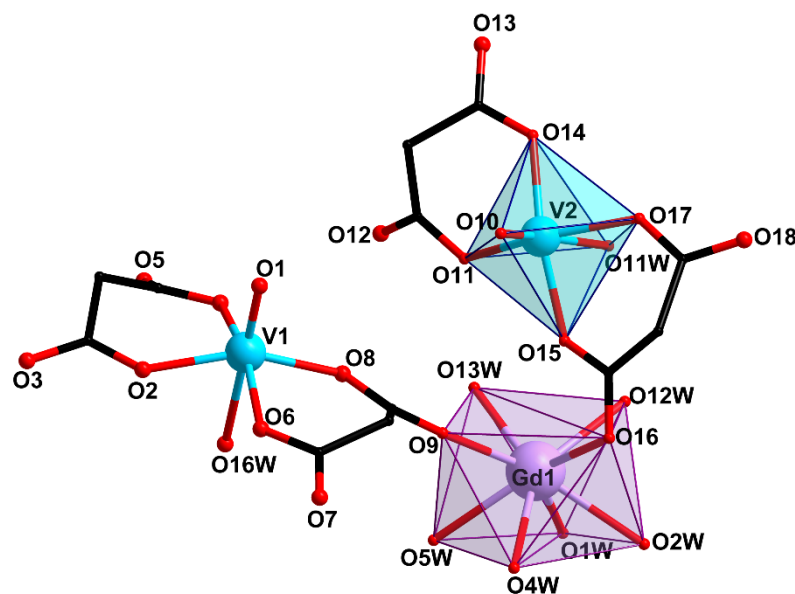


Figure 3. Structure of trinuclear unit $\{\text{GdV}_2\}^-$ in compound **3** (H atoms and cyclic fragments of the carboxylate ligands are not shown).

The coordination polyhedra of gadolinium (GdO_8) in **1–3** were analyzed using the SHAPE v2.1 program [46]. In **1**, the GdO_8 coordination polyhedron corresponded to a triangular dodecahedron [47] formed by six O atoms of water molecules (O11, O12, O13) and two O atoms of carboxylate groups (O7) (Figure 1, Table S4). The GdO_8 polyhedron in **2** can be described as a biaugmented (two-capped) trigonal prism [47] with the basal planes formed by the O5, O8W, and O10W atoms on the one side, and the O18, O6W, and O13W atoms on the other side. The caps of the trigonal prism were formed by the O7W and O9W atoms located above the O6W–O8W–O10W–O13W and O5–O18–O6W–O8W faces, respectively (Figure 2, Table S4). The geometry of the GdO_8 coordination polyhedron in **3** was closest to a tetragonal antiprism [47] with the basal planes formed by eight O atoms: four O atoms of water molecules (O1W, O2W, O4W, O5W) on the one side, and two O atoms of carboxylate groups (O9, O16) and two O atoms of water molecules (O12W, O13W) on the other side (Figure 3, Table S4).

In **1**, the $\{\text{GdV}_2\}^-$ units were linked in a 1D-polymeric chain by Na atoms coordinating the O atoms of carboxylate groups (O1 and O3) and water molecules (O6) belonging to the $\{(\text{VO})(\text{cbdc})_2(\text{H}_2\text{O})\}$ moieties of the neighboring $\{\text{GdV}_2\}^-$ units (Figure 4, Tables 1 and S1). The shortest $\text{V}\cdots\text{V}$ distance was observed between two metal atoms of the adjacent $\{\text{GdV}_2\}^-$ units (6.234 Å). The water molecules coordinated to Gd (O11, O12, O13), V (O6), Na (O14) atoms, the O2, O3, O7, O8, O9, O10 carboxylate atoms, the O5 atoms of $\{\text{V}=\text{O}\}$ moiety, and the CH_2 groups of the cyclobutane moieties of the ligand were involved in the formation of intra- and intermolecular hydrogen bonds which additionally stabilized the crystal structure of **1** (Table S5).

In **2**, the $\{\text{GdV}_2\}^-$ units were linked into a 3D-polymeric structure by Rb atoms bonding the O3, O7 carboxylate atoms of the $\{(\text{V}(1)\text{O})(\text{cbdc})_2(\text{H}_2\text{O})\}$ moieties and the O10, O12, O13 carboxylate atoms of the $\{(\text{V}(2)\text{O})(\text{cbdc})_2(\text{H}_2\text{O})\}$ moieties, as well as the water molecules coordinated to the V2 (O3W) and Gd (O8W, O13W) atoms (Figure 5, Tables 1 and S2). Unlike the $\{[\text{KGd}(\text{VO})_2(\text{cbdc})_4(\text{H}_2\text{O})_9]\cdot 3.5\text{H}_2\text{O}\}_n$ structure obtained previously, in which the K atom additionally coordinated only one water molecule [45], the Rb atom in the structure of **2** bound two water molecules (O12W, O13W). The crystal structure of **2** was additionally stabilized by a network of hydrogen bonds formed by carboxylate O atoms (O10 and O17), water molecules coordinated to the V (O3W and O4W) and Gd (O9W, O10W, O13W) atoms, as well as solvate water molecules (O1W, O2W, O5W) (Table S6).

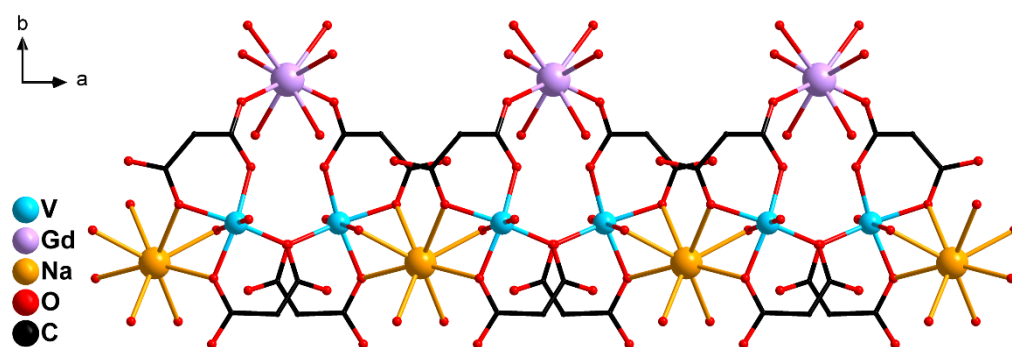


Figure 4. A fragment of 1D-polymeric chain of **1**: $\{\text{GdV}_2\}^-$ units linked by Na^+ cations (H atoms and cyclic fragments of the carboxylate ligands are not shown).

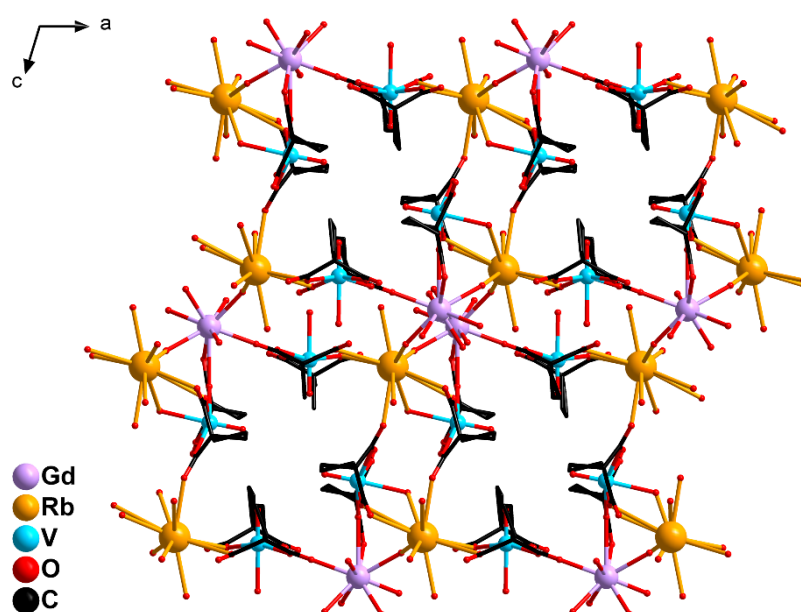


Figure 5. A fragment of 3D-polymeric structure of **2**: $\{\text{GdV}_2\}^-$ units linked by Rb^+ cations (H atoms are not shown).

In **3**, two Cs atoms were bound with two $\{\text{GdV}_2\}^-$ units via the O atoms of the carboxylate groups (O4, O8 and O12) and the water molecules coordinated to the V1 (O16W) and Gd (O13W) atoms. The Cs atoms connected the $\{\text{GdV}_2\}$ moieties into a dimer due to coordination of the carboxylate O13 atoms of the neighboring $\{\text{V}(2\text{O})(\text{cbdc})_2(\text{H}_2\text{O})\}$ moieties. Each Cs atom additionally coordinated three water molecules (O9W, O14W, O15W) (Figure 6, Tables 1 and S3). The crystal structure of **3** was stabilized by an extensive network of hydrogen bonds formed with participation of all coordinated and solvate water molecules and the O atoms of carboxylate groups (O2, O3, O5, O6, O7, O11, O12, O13, O14, O18) (Table S7).

Since the radius of Cs^+ ion is larger than that of Rb^+ , the former participated in linking not only with neighboring $\{\text{GdV}_2\}^-$ anions but also with nonequivalent bis-chelate moieties $\{\text{VO}(\text{cbdc})_2(\text{H}_2\text{O})\}$ within one $\{\text{GdV}_2\}^-$ unit. As a result, a decrease in the $\text{V}\cdots\text{V}$ distance (6.077 Å) was observed in the $\{\text{GdV}_2\}^-$ unit of **3** in comparison with that in **1** (6.391 Å) and **2** (7.010 Å), along with a sharp decrease in the dimensionality from 3D-polymeric to molecular structure. In addition, despite the structural similarity of the heterometallic trinuclear anions $\{\text{GdV}_2\}^-$ in all the three compounds, the presence in their structures of different alkali metal cations involved in linking the $\{\text{GdV}_2\}$ moieties to each other affected not only the structure dimensionality but also the $\text{V}\cdots\text{Gd}$ distances within the $\{\text{GdV}_2\}$ moieties (Figure 7).

resulting EPR spectra. Judging by the total spectrum width and shape, we concluded that the EPR spectrum was dominated by $S = 7/2$ signals of Gd^{III} with noticeable zero-field splitting. The signals of two V^{IV} ions with $S = 1/2$ had narrower spectra but much smaller integral intensity; therefore, they were buried in the much stronger signal of Gd^{III} (see Supplementary Materials for the supportive simulation).

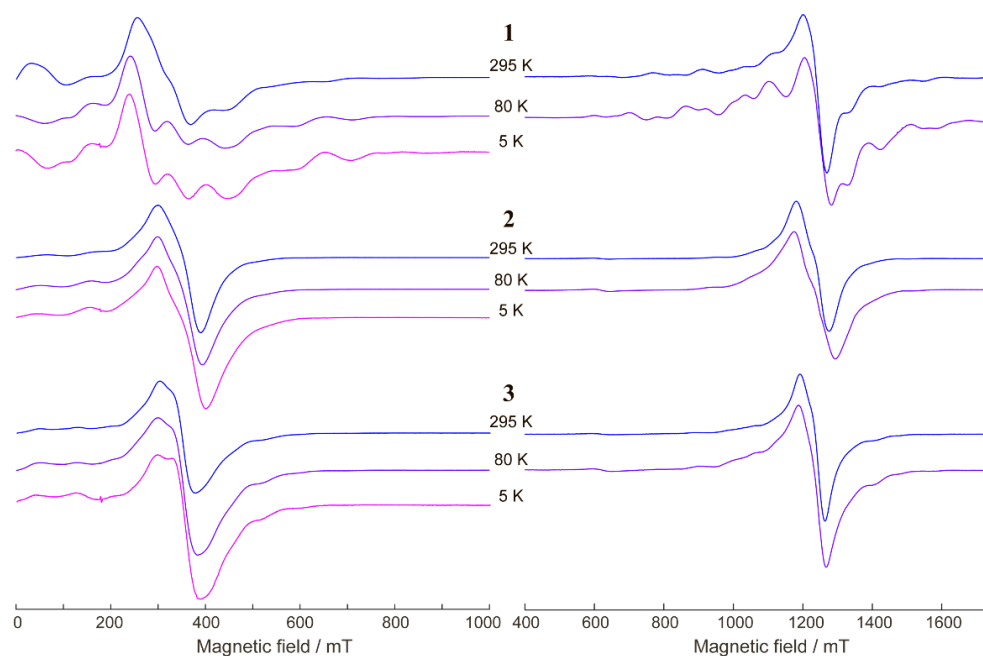


Figure 8. X-band (left) and Q-band (right) EPR spectra of 1–3 (as indicated) at $T = 295, 80,$ and 5 K. $\nu_{\text{mw}} \approx 9.75$ GHz at the X-band and $\nu_{\text{mw}} \approx 34.20$ GHz at the Q-band.

The zero-field splitting values D and E for **1** can be estimated simultaneously from the simulation of X/Q-band spectra (see Supplementary Materials). It was found that D was around ~ 0.08 cm^{-1} and $E/D \sim 0.1$ – 0.15 . For the two other compounds, **2** and **3**, the EPR spectra were less resolved (perhaps due to more efficient intermolecular exchange interactions), but it is obvious that the zero-field splitting had comparable or even smaller values.

2.4. Magnetic Properties

2.4.1. DC Susceptibility Measurements

The magnetic properties of compounds **1–3** were investigated by measuring the temperature dependences of molar magnetic susceptibility (χ_{M}) in the range of 2–300 K in a 5000 Oe *dc*-magnetic field. The experimental $\chi_{\text{M}}T$ values at 300 K for **1–3** (8.64, 8.74, and 8.89 $\text{cm}^3 \text{K mol}^{-1}$, respectively, see Figures 9–11) were similar to the spin-only value $\chi_{\text{M}}T_{\text{theor}} = 8.74$ $\text{cm}^3 \text{K mol}^{-1}$ expected for two non-interacting V^{IV} ions ($S = 1/2$) and one Gd^{III} ion ($S = 7/2$). The $\chi_{\text{M}}T(T)$ dependencies for **2** and **3** were similar in shape. The $\chi_{\text{M}}T$ values for **2** and **3** monotonically increased with decreasing temperature, reaching 8.99 and 9.03 $\text{cm}^3 \text{K mol}^{-1}$, respectively, at 45 K, then sharply grew to 9.75 and 9.71 $\text{cm}^3 \text{K mol}^{-1}$ at 4 K, and finally decreased to 8.63 and 9.03 $\text{cm}^3 \text{K mol}^{-1}$ at 2 K (Figures 9 and 10). The $\chi_{\text{M}}T$ value for **1** monotonically increased with cooling, reached 8.94 $\text{cm}^3 \text{K mol}^{-1}$ at 8 K, and then sharply decreased to 8.05 $\text{cm}^3 \text{K mol}^{-1}$ at 2 K (Figure 11).

The interpretation of the experimental plots of $\chi_{\text{M}}T$ vs. T for complexes **2** and **3** was carried out using PHI program [48] (for details see Supplementary Materials). The parameter of isotropic exchange between V^{IV} ions was neglected. The best fits of the experimental plots of $\chi_{\text{M}}T$ vs. T for **2** and **3** to the theoretically calculated curves were achieved with the following parameters: J_1 ($\text{Gd} \cdots \text{V1}$) = 0.989 ± 0.028 cm^{-1} , J_2 ($\text{Gd} \cdots \text{V2}$) = -0.089 ± 0.008 cm^{-1} , and $g = 2.01$ for **2** (Figure 9) and J_1 ($\text{Gd} \cdots \text{V1}$) = 0.656 ± 0.009 cm^{-1} , J_2 ($\text{Gd} \cdots \text{V2}$) = -0.050 ± 0.004 cm^{-1} , and $g = 2.03$ for **3** (Figure 10).

In order to clarify the correctness of the assignment of the J values to the V1-Gd and V2-Gd fragments in the compounds **2** and **3**, using a DFT method, we computationally considered two separate $\text{Gd}^{\text{III}}\{\text{VO}(\text{cbdc})_2(\text{H}_2\text{O})_8\}$ units of **2** and **3** and analyzed the forms of natural orbitals responsible for the character of the exchange interactions in $\text{V}^{\text{IV}}\text{-Gd}^{\text{III}}$ pairs of different type. Following from the shapes of natural orbitals (Figure S24), there was an overlapping of the orbitals of the gadolinium(III) and oxygen atom of the vanadium fragment $\{\text{V}(2)\text{O}(\text{cbdc})_2(\text{H}_2\text{O})_8\}$, which provided an exchange channel leading to antiferromagnetic coupling in $\text{V}(2)^{\text{IV}}\text{-Gd}^{\text{III}}$ pairs. In contrast, the orbitals of gadolinium and the closest oxygen atoms of $\{\text{V}(1)\text{O}(\text{cbdc})_2(\text{H}_2\text{O})_8\}$ did not overlap, which resulted in ferromagnetic interactions between V(1) and Gd.

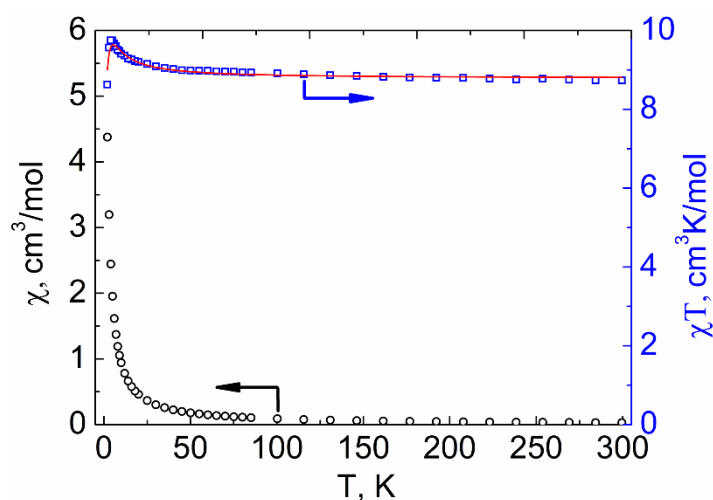


Figure 9. Temperature dependencies of the $\chi_{\text{M}}T$ product (\square) and χ_{M} (\circ) for compound **2**. The red line shows the values calculated using PHI [48] program.

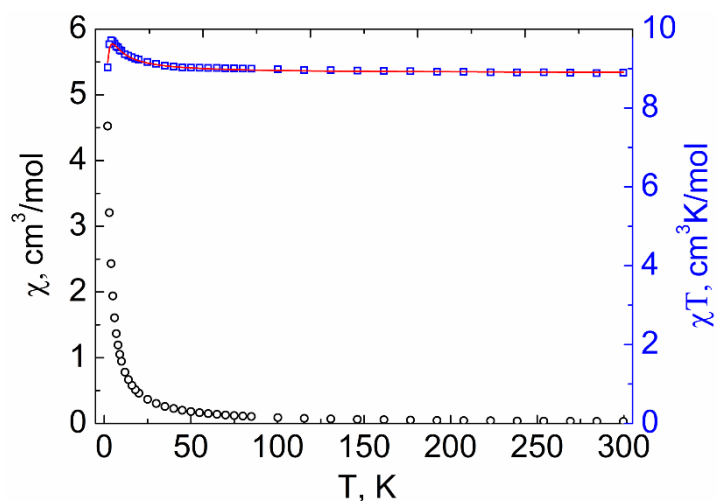


Figure 10. Temperature dependencies of the $\chi_{\text{M}}T$ product (\square) and χ_{M} (\circ) for compound **3**. The red line shows the values calculated using PHI [48] program.

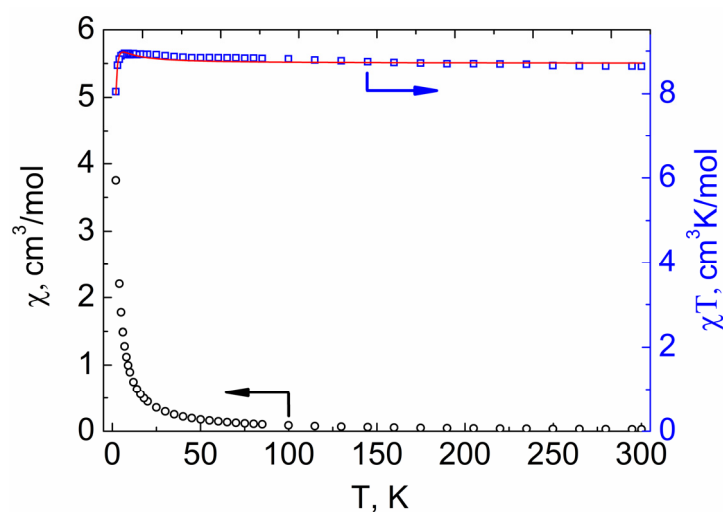


Figure 11. Temperature dependencies of the $\chi_M T$ product (\square) and χ_M (\circ) for compound **1**. The red line shows the values calculated using PHI [48] program.

For the interpretation of the temperature dependence of $\chi_M T$ for complex **1**, in addition to considering the magnetic exchange between Gd^{III} and V^{IV} ions, it is also necessary to take into account the exchange between V^{IV} ions belonging to neighboring $\{GdV_2\}^-$ units, which can interact through bridging Na^+ ions (for details see Supplementary Materials). The best fit of the experimental plot of $\chi_M T$ vs. T for **1**, obtained by the use of PHI [48] program, was achieved with the following parameters: $J_1 (Gd \cdots V) = 0.163 \pm 0.008 \text{ cm}^{-1}$, $J_2 (V \cdots V) = -1.095 \pm 0.046 \text{ cm}^{-1}$, $g = 2.01$.

There are several examples of Gd^{III} - V^{IV} O complexes in the literature for which the magnetic properties have been analyzed. The exchange parameters J_{GdV} obtained for **1–3** were within the range of known values (Table 2) where interactions between paramagnetic centers can be ferro- or antiferromagnetic, as determined by the nature of the bridging moieties and the interatomic distance.

Table 2. Magnetic properties of known Gd^{III} - V^{IV} complexes.

Complex	Distance $V \cdots Gd$, Å	Exchange Parameter J_{GdV} , cm^{-1}	Ref.
$\{[Gd(H_2O)_7(VO)_2(TTHA)][(VO)_2(TTHA)]_{0.5}\} \cdot 8.5H_2O$, $H_6TTHA = \text{triethylenetetraaminehexaacetic acid}$	6.099	-0.21	[30]
$[VO(L)Gd(hfa)_2(MeOH)]_2 \cdot 2MeOH \cdot 2Me_2CO$, $H_3L = 2\text{-hydroxy-N-}[(2\text{-hydroxyphenyl)methylene]amino\text{-}2\text{-methylpropyl benzamide}$	6.280	+0.46	[29]
$[L^1(VO)Gd(H_2O)(NO_3)_3] \cdot H_2O$, $H_2L^1 = N,N'$ -bis(3-methoxysalicylidene)-1,2-diamino-2-methylpropane	3.5191	+1.5	[27]
$[L^2(VO)(Me_2CO)Gd(NO_3)_3]$, $H_2L^2 = N,N'$ -bis(3-methoxysalicylidene)-1,3-diamino-2,2'-dimethylpropane	3.5043	-2.6	[28]
$[NaGd(VO)_2(cbdc)_4(H_2O)_{10}]_n$ (1)	5.722	$+0.163 \pm 0.008$	This work
$\{[RbGd(VO)_2(cbdc)_4(H_2O)_{10}] \cdot 2.5H_2O\}_n$ (2)	6.000 (V1) 4.611 (V2)	$+0.989 \pm 0.028$ -0.089 ± 0.008	This work
$\{[CsGd(VO)_2(cbdc)_4(H_2O)_{11}] \cdot 5H_2O\}_2$ (3)	6.290 (V1) 4.547 (V2)	$+0.656 \pm 0.009$ -0.050 ± 0.004	This work

2.4.2. AC Susceptibility Measurements

It is known that slow relaxation of the magnetization effect can be observed both for Gd^{III}- [36–44] and V^{IV}-based complexes [49–54]. This fact inspired us to perform *ac*-magnetic measurements for heterometallic Gd^{III}-V^{IV} compounds 1–3. As a result, all the synthesized complexes were found to exhibit field-induced slow relaxation of magnetization. However, in the zero *dc*-magnetic field, no out-of-phase signal was detected for 1–3 (Figures S13–S16). To suppress the quantum tunneling of the magnetization process (QTM), which appeared to be the most likely reason for the absence of relaxation under the zero *dc*-field, the subsequent *ac*-measurements were carried out in *dc*-fields from 500 to 5000 Oe. In this way, we managed to quantify the optimal *dc*-field values for 1–3. The highest relaxation times were achieved by applying the optimal fields of 5000 Oe for 1 (Figures S13 and S14), and 2500 Oe for 2 (Figure S15) and 3 (Figure S16). The optimal field was estimated at 8 K for 1, in contrast to 2 and 3 (2 K), because the low-temperature magnetic behavior of 1 under *ac*-field was quite difficult to explain.

To further study the relaxation dynamics, the isotherms of the in-phase and out-of-phase components of *ac*-magnetic susceptibility were measured for 1–3 under optimal H_{dc} fields (Figures S19–S21). To produce the temperature dependencies of relaxation time (τ vs. $1/T$) for 1–3, the $\chi''(\nu)$ isotherms were approximated by the generalized Debye model. The plots of τ vs. $1/T$ obtained in this way (Figure 12) were approximated by the equations corresponding to different relaxation mechanisms and their combinations (see Tables S14–S16 in Supplementary Material). The best-fit parameters for the approximations of τ vs. $1/T$ plots for 1–3 are presented in Table 4. In the high-temperature range, all the τ vs. $1/T$ dependences were approximated using only the Orbach relaxation mechanism ($\tau = \tau_0 \cdot \exp\{\Delta_{eff}/k_B T\}$) to estimate the value of the effective anisotropic barrier.

Table 3. The best-fit parameters of magnetization relaxation for 1_Y and 1_{Lu}.

Compound (Optimal <i>dc</i> -Field, Oe)	Orbach		Orbach + Raman				Orbach + Raman + QTM				
	$\Delta_{eff}/k_B, K$	τ_0, s	$\Delta_{eff}/k_B, K$	τ_0, s	$\frac{C_{Raman}}{s^{-1}K^{-n_{Raman}}}$	n_{Raman}	$\Delta_{eff}/k_B, K$	τ_0, s	$\frac{C_{Raman}}{s^{-1}K^{-n_{Raman}}}$	n_{Raman}	B, s^{-1}
1 _Y (5000)	76	$5.81 \cdot 10^{-6}$	-	-	-	-	22	$9 \cdot 10^{-5}$	26	1.8	207
1 _{Lu} (2500)	50	$1.0 \cdot 10^{-5}$	26	$9 \cdot 10^{-5}$	89	1.50	-	-	-	-	-

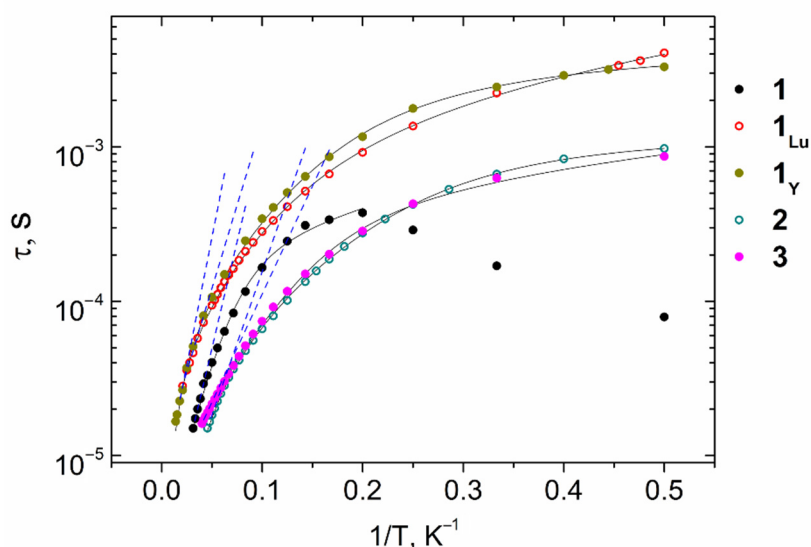


Figure 12. τ vs. $1/T$ dependences for complexes 1–3, 1_Y, and 1_{Lu} under H_{dc} fields of 2500 (2, 3, 1_{Lu}) and 5000 Oe (1, 1_Y). Blue dashed lines represent fittings of the high-temperature range by the Orbach mechanism. Black solid lines represent fittings by the combinations of relaxation mechanisms presented in Tables 3 and 4.

Table 4. The best-fit parameters of magnetization relaxation for 1–3.

Compound (Optimal <i>dc</i> -Field, Oe)	Orbach		Orbach + Direct			Orbach + Raman + QTM				
	Δ_{eff}/k_B , K	τ_0 , s	Δ_{eff}/k_B , K	τ_0 , s	$A_{\text{direct}}/K^{-1}\text{Oe}^{-4}\text{s}^{-1}$	Δ_{eff}/k_B , K	τ_0 , s	$C_{\text{Raman}}/s^{-1}\text{K}^{-n_{\text{Raman}}}$	n_{Raman}	B , s^{-1}
1 (5000)	63	$2 \cdot 10^{-6}$	60	$3 \cdot 10^{-6}$	$8.0 \cdot 10^{-13}$	-	-	-	-	-
2 (2500)	43	$2 \cdot 10^{-6}$	-	-	-	15	$4.3 \cdot 10^{-5}$	44	2.32	794
3 (2500)	32	$4 \cdot 10^{-6}$	27	$8 \cdot 10^{-6}$	$1.43 \cdot 10^{-11}$	-	-	-	-	-

The best approximations of τ vs. $1/T$ dependences for complexes **1** and **3** were achieved using the Orbach and direct relaxation mechanisms ($\tau^{-1} = \tau_0^{-1} \cdot \exp(-\Delta_{\text{eff}}/k_B T) + A_{\text{direct}} T H^4$). The other combinations of the two relaxation mechanisms, as well as the single Orbach and Raman mechanisms, failed to fit the high-temperature range of the experimental data. The addition of a third relaxation mechanism led to overparameterization in all cases. In contrast, an ensemble of the Orbach, Raman, and QTM relaxation mechanisms ($\tau^{-1} = \tau_0^{-1} \exp(-\Delta_{\text{eff}}/k_B T) + C_{\text{Raman}} T^{n_{\text{Raman}}} + B$) was used for the best-fit of the experimental data for **2**. Adjunction of the third relaxation mechanism in this instance resulted in an improvement of the approximation in comparison with all options involving two relaxation mechanisms.

In our previous paper [55], we reported on two structural analogs of **1**, $[\text{NaLn}(\text{VO})_2(\text{cbdc})_4(\text{H}_2\text{O})_{10}]_n$ (**1_Y**: Ln = Y, **1_{Lu}**: Ln = Lu). However, the SMM properties of those compounds were thoroughly studied in the present study (Figures S17, S18, S22 and S23). The corresponding fitting parameters of the τ vs. $1/T$ plots (Figure 12) are presented below (Table 3). The $\tau(1/T)$ best-fits in the entire temperature range for **1_Y** and **1_{Lu}** were achieved using the cooperative contribution of Orbach and Raman mechanisms ($\tau^{-1} = \tau_0^{-1} \cdot \exp(-\Delta_{\text{eff}}/k_B T) + C_{\text{Raman}} T^{n_{\text{Raman}}}$) for **1_{Lu}** and the Orbach, Raman, and QTM mechanisms for **1_Y**. Other combinations of relaxation mechanisms either failed to fit the experimental data or led to over-parametrization.

At low temperatures, the relaxation of **1** was strikingly different from the relaxation of **2** and **3**. A decrease in the relaxation time with a temperature decrease was observed. Because of this, the low-temperature section of the τ vs. $1/T$ plot cannot be approximated by a sum of any relaxation mechanisms. Such a change may originate from the absence of a network of hydrogen bonds in **1**, in contrast to the structures of compounds **2** and **3**.

The minimum V...V distance (6.077 Å) and one of the Gd...V distances (4.547 Å) in compound **3** led to the largest dipole-dipole interaction between ions in the Gd^{III}...V^{IV} and V^{IV}...V^{IV} pairs. These interactions possibly give rise to additional pathways of magnetization relaxation, and hence acceleration of relaxation [56]. Therefore, for compound **3**, the effective magnetization reversal barrier, estimated from the high-temperature section by the Arrhenius equation, was the smallest.

Thus, as follows from a comparison of *ac*-magnetic data for **1**, **1_Y**, and **1_{Lu}**, the slow relaxation of magnetization in Gd^{III}-V^{IV} compounds can be determined by the contributions of both Gd^{III} and V^{IV} ions. Moreover, compounds **1**, **1_Y**, and **1_{Lu}** demonstrated the highest Δ_{eff} values (according to the approximation by a single Orbach mechanism) compared with those of **2** and **3**, which can be explained by longer V...V (6.234 Å for **1** and 6.216 Å for **1_Y**) and Gd...V distances (5.722 Å for **1**) weakening the dipole-dipole interaction between paramagnetic ions.

3. Materials and Methods

3.1. Synthesis

3.1.1. General Details

The synthesis of new compounds was carried out in air using distilled water. The following starting reagents were purchased from commercial sources and used without further purification: VOSO₄·3H₂O (>99%), Ba(NO₃)₂ (>98%), H₂cbdc (99%, Acros Organics), Gd(NO₃)₃·6H₂O (99.9%, Lanhit), NaOH (>99%), RbOH·xH₂O (Sigma Aldrich), and CsOH·H₂O (99.95%, Acros Organics). The complexes $[\text{NaLn}(\text{VO})_2(\text{cbdc})_4(\text{H}_2\text{O})_{10}]_n$

(**1_Y**: Ln = Y, **1_{Lu}**: Ln = Lu) were synthesized according to procedures described previously [56]. The IR spectra of complexes **1–3** were measured using a Spectrum 65 FT-IR spectrometer (Perkin-Elmer) by the ATR method in the range of 4000–400 cm⁻¹. Elemental C,H,N-analysis was carried out using an EuroEA 3000 automatic analyzer (EuroVector).

3.1.2. Synthetic Procedure

The solution of VOSO₄·3H₂O (0.150 g, 0.69 mmol) in H₂O (15 mL) was added with crystalline Ba(NO₃)₂ (0.181 g, 0.69 mmol), and the reaction mixture was stirred for 25 min at 23 °C. Weight amounts of H₂cbdc (0.199 g, 1.38 mmol) and corresponding alkaline metal hydroxide (NaOH, 0.110 g, 2.76 mmol for **1**; RbOH·xH₂O, 0.283 g, 2.76 mmol for **2**; CsOH·H₂O, 0.414 g, 2.76 mmol for **3**) were dissolved in H₂O (10 mL) at 40 °C, and the resulting clear solution of M₂(cbdc) was poured into the reaction mixture. The stirring was continued for 15 min, and crystalline Gd(NO₃)₃·6H₂O (0.311 g, 0.69 mmol) was added. After 15 min, the reaction mixture was left for 1 h without disturbance. The BaSO₄ precipitate was filtered off, and the resulting sky-blue solution (25 mL) was left to evaporate in air at 23 °C. Blue crystals precipitated in 3 weeks were suitable for X-ray diffraction. The crystals were filtered from the mother liquor, washed with H₂O (*t* = 5 °C), and dried in air at 23 °C.

For [NaGd(VO)₂(cbdc)₄(H₂O)₁₀]_{*n*} (**1**): the yield was 0.199 g (54.3 % based on VOSO₄·3H₂O). Calc. (%) for C₂₄H₄₄GdNaO₂₈V₂: C, 27.12; H, 4.17. Found (%) C, 27.04; H, 4.17. IR spectrum (ATR, ν/cm⁻¹) (s = strong, m = medium, w = weak): 3643 v. w, 3347 m. br [ν(O–H)], 3227 w. br [ν(O–H)], 2999 w [ν(C–H)], 2956 w [ν(C–H)], 1634 w, 1579 s [ν_{as}(COO⁻)], 1553 s [ν_{as}(COO⁻)], 1443 m, 1431 m, 1390 s [ν_s(COO⁻)], 1348 s, 1253 w, 1244 w, 1229 m [ν(C–C)cycle], 1162 w, 1122 m [γ(C(–C)₂)], 1063 w, 1011 w, 1000 w, 968 s [ν(V=O)], 952 m, 924 m, 876 w, 843 w, 808 w, 773 m, 725 s [δ(COO⁻)], 640 s, 561 s, 532 s, 467 s, 443 s, 420 s.

For [[RbGd(VO)₂(cbdc)₄(H₂O)₁₀].2.5H₂O]_{*n*} (**2**): the yield was 0.113 g (28 % based on VOSO₄·3H₂O). Calc. (%) for C₂₄H₄₉GdRbO_{30.5}V₂: C, 24.63; H, 4.22. Found (%): C, 24.68; H, 4.50. IR spectrum (ATR, ν/cm⁻¹) (s = strong, m = medium, w = weak): 3576 v. w, 3243 m. br [ν(O–H)], 3018 w [ν(C–H)], 2973 w [ν(C–H)], 2873 w, 1666 w, 1559 s [ν_{as}(COO⁻)], 1533 s [ν_{as}(COO⁻)], 1457 m, 1431 s, 1401 s [ν_s(COO⁻)], 1379 s [ν_s(COO⁻)], 1357 s, 1342 s, 1259 w, 1228 m [ν(C–C)cycle], 1169 w, 1124 m [γ(C(–C)₂)], 1060 v. w, 1008 w, 994 s [ν(V=O)], 984 s [ν(V=O)], 961 w, 917 s, 879 w, 863 w, 776 s, 763 s [δ(COO⁻)], 734 s, 709 s [δ(COO⁻)], 654 s, 552 s, 537 s, 453 s, 433 s, 420 s.

For [[CsGd(VO)₂(cbdc)₄(H₂O)₁₁].5H₂O]_{*n*} (**3**): the yield was 0.097 g (32.8 % based on VOSO₄·3H₂O). Calc. (%) for C₂₄H₅₆CsGdO₃₄V₂: C, 22.50; H, 4.41. Found (%): C, 22.47; H, 4.49. IR spectrum (ATR, ν/cm⁻¹) (s = strong, m = medium, w = weak): 3311 m. br, 3215 m. br [ν(O–H)], 3027 w, 3006 m [ν(C–H)], 2986 w [ν(C–H)], 2969 w [ν(C–H)], 1627 m, 1557 s [ν_{as}(COO⁻)], 1455 m, 1404 s [ν_s(COO⁻)], 1386 s [ν_s(COO⁻)], 1353 s, 1307 m, 1256 w, 1244 w, 1227 w [ν(C–C)cycle], 1182 w, 1163 w, 1126 w [γ(C(–C)₂)], 1063 w, 1047 v. w, 1015 w, 998 w, 988 s [ν(V=O)], 976 s [ν(V=O)], 960 m, 934 w, 916 w, 882 m, 856 m, 781 s [δ(COO⁻)], 762 s [δ(COO⁻)], 696 s, 653 s, 615 s, 595 s, 546 s, 466 s, 449 s.

3.2. Single Crystal X-ray Diffraction

Single crystal X-ray diffraction study for the crystals of **1–3** was carried out on a Bruker SMART APEX II diffractometer equipped with a CCD detector (Mo-K_α, λ = 0.71073 Å, graphite monochromator) [57]. Semi-empirical absorption correction was applied by the SADABS program [58]. The structures were solved by direct methods and refined by the full-matrix least squares in the anisotropic approximation for non-hydrogen atoms. The calculations were carried out by the SHELX-2014 program package [59] using Olex2 1.2 [60]. The hydrogen atoms in structures **1–3** were positioned geometrically and refined using the riding model. The crystallographic parameters for **1–3** and the structure refinement details are given in Table 5.

Table 5. Crystallographic parameters and structure refinement details for compounds 1–3.

Parameter	1	2	3
Empirical formula	C ₂₄ H ₄₀ GdNaO ₂₈ V ₂	C ₂₄ H ₄₉ GdO _{30.5} RbV ₂	C ₂₄ H ₅₆ CsGdO ₃₄ V ₂
<i>T</i> /K	150(2)	120	120
Formula weight (g·mol ^{−1})	1058.68	1170.23	1280.72
Crystal system	monoclinic	monoclinic	triclinic
Space group	C2/c	C2/c	P $\bar{1}$
<i>a</i> (Å)	9.0936 (2)	23.375 (2)	12.0203 (14)
<i>b</i> (Å)	24.7129 (5)	13.2166 (12)	13.3110 (15)
<i>c</i> (Å)	17.1366 (4)	26.305 (2)	14.3630 (17)
α (deg)	90	90	110.948 (2)
β (deg)	104.7320 (10)	106.853 (2)	92.627 (2)
γ (deg)	90	90	97.051 (2)
<i>V</i> (Å ³)	3724.49 (14)	7777.7 (12)	2120.0 (4)
<i>Z</i>	4	8	2
<i>D</i> _{calc} (g·cm ^{−3})	1.888	1.999	2.006
θ_{\min} – θ_{\max} (deg)	2.366	3.507	2.934
μ (mm ^{−1})	2.46–30.51	2.23–33.72	2.18–30.41
Number of measured reflections	20,747	52,901	20,664
Number of reflections with <i>I</i> > 2 σ (<i>I</i>)	4643	9629	6790
<i>R</i> _{int}	0.0339	0.0588	0.0488
<i>Goof</i>	1.045	1.024	1.037
<i>R</i> ₁ ^[a] , <i>wR</i> ₂ ^[b] (<i>I</i> > 2 σ (<i>I</i>))	0.0276, 0.0756	0.0367, 0.0774	0.0377, 0.0824
<i>R</i> ₁ ^[a] , <i>wR</i> ₂ ^[b] (all data)	0.0303, 0.0773	0.0513, 0.0839	0.0507, 0.0900
<i>T</i> _{min} / <i>T</i> _{max}	0.718/0.833	0.429/0.526	0.533/0.746

^[a] $R_1 = \sum ||F_\sigma| - |F_c|| / \sum |F_o|$. ^[b] $wR_2 = [\sum w(F_o^2 - F_c^2)^2 / \sum w(F_o^2)^2]^{1/2}$.

CCDC 2019386–2019388 contain supplementary crystallographic data for 1–3. These data can be obtained free of charge via <http://www.ccdc.cam.ac.uk/conts/retrieving.html>, or from the Cambridge Crystallographic Data Centre, 12 Union Road, Cambridge, CB2 1EZ, UK; fax: (+44) 1223-336-033; or e-mail: deposit@ccdc.cam.ac.uk.

3.3. Powder X-ray Diffraction

The purity of the samples for magnetic measurements and EPR spectroscopy was achieved by powder X-ray diffraction. The powder patterns were obtained at room temperature on a Bruker D8 Advance diffractometer with a LynxEye detector in Bragg-Brentano geometry, with the sample dispersed thinly on a zero-background Si sample holder, $\lambda(\text{CuK}\alpha) = 1.54060 \text{ \AA}$, θ/θ scan with variable slits (irradiated length 20 mm) from 4° to 65° 2 θ , step size 0.020° (Figures S25–S27).

3.4. EPR Spectroscopy

Variable-temperature continuous wave X/Q-band EPR spectra were obtained using a Bruker Elexsys E580 spectrometer equipped with an Oxford Instruments temperature control system (*T* = 4–300 K). All spectral simulations were done using the EasySpin toolbox for Matlab [61].

3.5. Magnetic Measurements

Magnetic susceptibility measurements were performed with a Quantum Design PPMS-9 susceptometer. *Dc*-magnetic susceptibility measurements were performed in the 2–300 K temperature range in a 5000 Oe *dc*-magnetic field. For *ac*-susceptibility measurements, oscillating *ac*-magnetic fields of 5, 3, and 1 Oe within frequency ranges 10–100, 100–1000, and 1000–10,000 Hz, respectively, were applied. Measurements were performed on polycrystalline samples sealed in a polyethylene bag and covered with mineral oil in order to prevent field-induced orientation of the crystals. Magnetic data were corrected

for the diamagnetic contribution evaluated from Pascal's constants, the sample holder, and mineral oil.

3.6. DFT Calculations

The density functional theory calculations were performed by using the Gaussian 09 program package [62] with the UB3LYP functional [63]. The standard 6-31G (d,p) basis set was used for all atoms with the exception of Gd, for which the SDD basis set with effective core potential was employed. The relativistic effects were incorporated via the Douglas-Kroll-Hess (DKH) [64,65] method.

4. Conclusions

The radius of the alkali metal cation (Na, Rb, Cs) was shown to affect the structure of trinuclear heterometallic anions $[\text{Gd}(\text{VO})_2(\text{cbdc})_4(\text{H}_2\text{O})_8]^-$ and their mutual arrangement in a crystal. With Na^+ , trinuclear $[\text{GdV}_2]^-$ moieties were characterized by identical $\text{V}\cdots\text{Gd}$ distances and were connected into 1D-polymeric chains in the case of **1**. With Rb^+ and Cs^+ , the $\text{V}\cdots\text{Gd}$ distances were different, and $[\text{GdV}_2]^-$ fragments were linked into a 3D-framework for **2** and a molecular complex for **3**, respectively. Based on EPR spectroscopy data for **1**, the presence of weak magnetic anisotropy of Gd^{III} ions was identified ($D\sim 0.08\text{ cm}^{-1}$ and $E/D\sim 0.1\text{--}0.15$). Fitting the $\chi_{\text{M}}T$ -temperature plots (excluding the magnetic anisotropy contributions of metal ions) showed the presence of ferromagnetic exchange interactions between Gd^{III} and V^{IV} ions in the trinuclear unit of **1**, and both ferro- and antiferromagnetic exchange channels in **2** and **3**. AC-susceptibility measurements showed field-induced slow relaxation of magnetization in **1–3** that can be described using the sum of Orbach and direct mechanisms for **1** and **3**, or the sum of Orbach, Raman, and QTM mechanisms for **2**. Moreover, of all the compounds obtained, the highest values of the effective anisotropic energy barrier (according to the approximation by a single Orbach mechanism) were obtained for **1** and its structural analogs with diamagnetic Y^{III} and Lu^{III} ions.

Supplementary Materials: The following are available online at <https://www.mdpi.com/article/10.3390/magnetochemistry7060082/s1>: Table S1–S3: Selected bond lengths and angles for **1–3**, Table S4: Continuous shape measures (CSHM) for GdO_8 coordination polyhedra in compounds **1–3**, Figure S1: EPR spectra of **1** at $T = 80\text{ K}$, Figure S2: Simulation of the anticipated contributions of $\text{Gd}(\text{III})$ ion and two $\text{V}(\text{IV})$ ions into the overall EPR spectrum, Tables S5–S7: Hydrogen bonding parameters of structures **1–3**, Figures S3–S5: Fitting the experimental $1/\chi_{\text{M}}$ vs. T plots, Figures S6–S11 and Tables S8–S13: Fitting the experimental curves $\chi_{\text{M}}T$ vs. T for complexes **1–3**, Figure S12: Fitting the experimental curve $\chi_{\text{M}}T$ vs. T for complex **1_{Lu}**, Figures S13–S23: AC magnetic data, Tables S14–S16: Fitting of the τ vs. $1/T$ dependences for **1–3**; Figure S24: Natural orbitals of $\text{V}^{\text{IV}}\text{-Gd}^{\text{III}}$ fragments of the compounds **2** and **3** calculated by the DFT method, Figures S25–S27: PXRD data.

Author Contributions: Conceptualization, methodology, E.S.B., M.A.K. and I.L.E.; formal analysis, J.K.V., A.A.K., K.A.B., E.A.U., N.N.E. and M.V.F.; investigation, validation, E.S.B., J.K.V., A.A.K., K.A.B., N.N.E. and M.V.F.; writing—original draft preparation, E.S.B., K.A.B., E.A.U. and M.V.F.; writing—review and editing, E.S.B., N.N.E., M.A.K. and I.L.E.; visualization, E.S.B., K.A.B., M.V.F. and M.A.K.; supervision, M.A.K. and I.L.E. All authors have read and agreed to the published version of the manuscript.

Funding: This study was funded by the Russian Science Foundation, grant number 19-73-10181.

Institutional Review Board Statement: Not applicable.

Informed Consent Statement: Not applicable.

Data Availability Statement: The data presented in this study are available in this article and supplementary materials.

Acknowledgments: Single-crystal X-ray diffraction analysis for **1**, powder X-ray diffraction analysis, IR spectroscopy, CHN analysis, and magnetic measurements for **1–3** were performed using the equipment of the JRC PMR IGIC RAS. X-ray diffraction data for **2** and **3** were collected using the

equipment of Center for molecular composition studies of INEOS RAS. We are grateful to the Ministry of Science and Higher Education of the Russian Federation for the access to EPR equipment. We are grateful to Maxim A. Shmelev for the XPRD experiments and Alyona A. Starikova for the help with DFT calculations.

Conflicts of Interest: The authors declare no conflict of interest.

References

1. Zhang, R.; Wang, L.; Xu, C.; Yang, H.; Chen, W.; Gao, G.; Liu, W. Anion-induced 3d-4f luminescent coordination clusters: Structural characteristics and chemical fixation of CO₂ under mild conditions. *Dalton Trans.* **2018**, *47*, 7159–7165. [[CrossRef](#)]
2. Li, L.; Zou, J.-Y.; You, S.-Y.; Cui, H.-M.; Zeng, G.-P.; Cui, J.-Z. Tuning the luminescence of two 3d-4f metal-organic frameworks for the fast response and highly selective detection of aniline. *Dalton Trans.* **2017**, *46*, 16432–16438. [[CrossRef](#)]
3. Dey, A.; Acharya, J.; Chandrasekhar, V. Heterometallic 3d-4f Complexes as Single—Molecule Magnets. *Chem. Asian J.* **2019**, *14*, 4433–4453. [[CrossRef](#)]
4. Dey, A.; Bag, P.; Kalita, P.; Chandrasekhar, V. Heterometallic Cu^{II}-Ln^{III} complexes: Single molecule magnets and magnetic refrigerants. *Coord. Chem. Rev.* **2021**, *432*, 213707. [[CrossRef](#)]
5. Yin, J.-J.; Lu, T.-Q.; Chen, C.; Zhuang, G.-L.; Zheng, J.; Zheng, X.-Y.; Shao, F. Magnetocaloric Effect and Slow Magnetic Relaxation on Two Dimensional Layered 3d-4f Cluster-Based Metal-Organic Frameworks. *Cryst. Growth Des.* **2020**, *20*, 4005–4012. [[CrossRef](#)]
6. Cremades, E.; Gómez-Coca, S.; Aravena, D.; Alvarez, S.; Ruiz, E. Theoretical Study of Exchange Coupling in 3d-Gd Complexes: Large Magnetocaloric Effect Systems. *J. Am. Chem. Soc.* **2012**, *134*, 10532–10542. [[CrossRef](#)]
7. Lin, Q.; Li, J.; Dong, Y.; Zhou, G.; Song, Y.; Xu, Y. Lantern-shaped 3d–4f high-nuclearity clusters with magnetocaloric effect. *Dalton Trans.* **2017**, *46*, 9745–9749. [[CrossRef](#)] [[PubMed](#)]
8. Liu, C.-M.; Zhang, D.-Q.; Hao, X.; Zhu, D.-B. Assembly of chiral 3d–4f wheel-like cluster complexes with achiral ligands: Single—molecule magnetic behavior and magnetocaloric effect. *Inorg. Chem. Front.* **2020**, *7*, 3340–3351. [[CrossRef](#)]
9. Oyarzabal, I.; Echenique-Errandonea, E.; San Sebastián, E.; Rodríguez-Diéguez, A.; Seco, J.M.; Colacio, E. Synthesis, Structural Features and Physical Properties of a Family of Triply Bridged Dinuclear 3d-4f Complexes. *Magnetochemistry* **2021**, *7*, 22. [[CrossRef](#)]
10. Griffiths, K.; Kostakis, G.E. Transformative 3d-4f coordination cluster carriers. *Dalton Trans.* **2018**, *47*, 12011–12034. [[CrossRef](#)] [[PubMed](#)]
11. Kumar, P.; Griffiths, K.; Anson, C.E.; Powell, A.K.; Kostakis, G.E. A tetranuclear Cu^{II}Dy^{III}₂ coordination cluster as a Suzuki (C–C) coupling reaction promoter. *Dalton Trans.* **2018**, *47*, 17202–17205. [[CrossRef](#)]
12. Cancino, P.; Santibañez, L.; Stevens, C.; Fuentealba, P.; Audebrand, N.; Aravena, D.; Torres, J.; Martinez, S.; Kremere, C.; Spodine, E. Influence of the channel size of isostructural 3d-4f MOFs on the catalytic aerobic oxidation of cycloalkenes. *New J. Chem.* **2019**, *43*, 11057–11064. [[CrossRef](#)]
13. Dermitzaki, D.; Psycharis, V.; Sanakis, Y.; Stamatatos, T.C.; Pissas, M.; Raptopoulou, C.P. Extending the family of heptanuclear heterometallic Cu₅Ln₂ (Ln = Gd, Tb, Dy) complexes: Synthesis, crystal structures, magnetic and magnetocaloric studies. *Polyhedron* **2019**, *169*, 135–143. [[CrossRef](#)]
14. Zhang, H.-G.; Yang, H.; Sun, L.; Li, D.-C.; Dou, J.-M. A New Family of 2D Coordination Polymers Based on 3d–4f 15—Metallacrown-5 Units: Synthesis, Structure, and Single-Molecule Magnet Behavior. *Eur. J. Inorg. Chem.* **2019**, *2019*, 2839–2843. [[CrossRef](#)]
15. Worrell, A.; Sun, D.; Mayans, J.; Lampropoulos, C.; Escuer, A.; Stamatatos, T.C. Oximate-Based Ligands in 3d/4f-Metal Cluster Chemistry: A Family of {Cu₃Ln} Complexes with a “Propeller”-like Topology and Single-Molecule Magnetic Behavior. *Inorg. Chem.* **2018**, *57*, 13944–13952. [[CrossRef](#)]
16. Zhao, X.; Li, G.; Ma, J.; Liu, W. Two Octanuclear {Cu₄Ln₄} (Ln = Dy or Tb) Complexes with a Butterfly-Shaped Unit Exhibiting Zero-Field Single-Molecule Magnet Behavior. *Inorg. Chem.* **2020**, *59*, 2328–2336. [[CrossRef](#)] [[PubMed](#)]
17. Shi, J.Y.; Chen, P.Y.; Wu, M.Z.; Tian, L.; Liu, Z.Y. Synthesis of a series of hetero-multi-spin Ln₂Cu₃ complexes based on a methyl-pyrazole nitronyl nitroxide radical with slow magnetic relaxation behaviors. *Dalton Trans.* **2019**, *48*, 9187–9193. [[CrossRef](#)]
18. Ghosh, T.K.; Maity, S.; Mayans, J.; Ghosh, A. Family of Isomeric Cu^{II}-Ln^{III} (Ln = Gd, Tb, and Dy) Complexes Presenting Field-Induced Slow Relaxation of Magnetization Only for the Members Containing Gd^{III}. *Inorg. Chem.* **2021**, *60*, 438–448. [[CrossRef](#)]
19. Liu, J.-L.; Lin, W.-Q.; Chen, Y.-C.; Gómez-Coca, S.; Aravena, D.; Ruiz, E.; Leng, J.-D.; Tong, M.-L. Cu^{II}-Gd^{III} Cryogenic Magnetic Refrigerants and Cu₈Dy₉ Single-Molecule Magnet Generated by In Situ Reactions of Picolinaldehyde and Acetylpyridine: Experimental and Theoretical Study. *Chem. Eur. J.* **2013**, *19*, 17567–17577. [[CrossRef](#)]
20. Singh, M.K.; Rajeshkumar, T.; Kumar, R.; Singh, S.K.; Rajaraman, G. Role of (1,3) {Cu–Cu} Interaction on the Magneto-Caloric Effect of Trinuclear {Cu^{II}-Gd^{III}-Cu^{II}} Complexes: Combined DFT and Experimental Studies. *Inorg. Chem.* **2018**, *57*, 1846–1858. [[CrossRef](#)] [[PubMed](#)]
21. Alexandropoulos, D.I.; Poole, K.M.; Cunha-Silva, L.; Sheikh, J.A.; Wernsdorfer, W.; Christou, G.; Stamatatos, T.C. A family of ‘windmill’-like {Cu₆Ln₁₂} complexes exhibiting single-molecule magnetism behavior and large magnetic entropy changes. *Chem. Commun.* **2017**, *53*, 4266–4269. [[CrossRef](#)] [[PubMed](#)]

22. Dey, A.; Das, S.; Palacios, M.A.; Colacio, E.; Chandrasekhar, V. Single-Molecule Magnet and Magnetothermal Properties of Two-Dimensional Polymers Containing Heterometallic $[\text{Cu}_5\text{Ln}_2]$ ($\text{Ln} = \text{Gd}^{\text{III}}$ and Dy^{III}) Motifs. *Eur. J. Inorg. Chem.* **2018**, *2018*, 1645–1654. [[CrossRef](#)]
23. Alexandropoulos, D.I.; Cunha-Silva, L.; Tang, J.; Stamatatos, T.C. Heterometallic Cu/Ln cluster chemistry: Ferromagnetically-coupled $\{\text{Cu}_4\text{Ln}_2\}$ complexes exhibiting single-molecule magnetism and magnetocaloric properties. *Dalton Trans.* **2018**, *47*, 11934–11941. [[CrossRef](#)] [[PubMed](#)]
24. Kettles, F.J.; Milway, V.A.; Tuna, F.; Valiente, R.; Thomas, L.H.; Wernsdorfer, W.; Ochsenein, S.T.; Murrie, M. Exchange Interactions at the Origin of Slow Relaxation of the Magnetization in $\{\text{TbCu}_3\}$ and $\{\text{DyCu}_3\}$ Single-Molecule Magnets. *Inorg. Chem.* **2014**, *53*, 8970–8978. [[CrossRef](#)] [[PubMed](#)]
25. Kong, J.-J.; Zhang, J.-C.; Jiang, Y.-X.; Tao, J.-X.; Wang, W.-Y.; Huang, X.-C. Two-dimensional heterometallic $\text{Cu}^{\text{II}}\text{Ln}^{\text{III}}$ ($\text{Ln} = \text{Tb}$ and Dy) coordination polymers bridged by dicyanamides showing slow magnetic relaxation behavior. *CrystEngComm* **2019**, *21*, 5145–5151. [[CrossRef](#)]
26. Chen, Y.; Long, Q.-Q.; Hu, Z.-B.; Wang, H.-S.; Huang, Z.-Y.; Chen, W.; Song, Y.; Zhang, Z.-C.; Yang, F.-J. Synthesis, crystal structures and magnetic properties of a series of pentanuclear heterometallic $[\text{Cu}^{\text{II}}_3\text{Ln}^{\text{III}}_2]$ ($\text{Ln} = \text{Ho}$, Dy , and Gd) complexes containing mixed organic ligands. *New J. Chem.* **2019**, *43*, 8101–8108. [[CrossRef](#)]
27. Costes, J.-P.; Dupuis, A.; Laurent, J.-P. An original heterodinuclear VO^{2+} , Gd^{3+} complex with a nonet ground state. *J. Chem. Soc. Dalton Trans.* **1998**, 735–736. [[CrossRef](#)]
28. Costes, J.-P.; Dahan, F.; Donnadieu, B.; Garcia-Tojal, J.; Laurent, J.-P. Versatility of the Nature of the Magnetic Gadolinium(III)–Vanadium(IV) Interaction—Structure and Magnetic Properties of Two Heterobinuclear $[\text{Gd}, \text{V}(\text{O})]$ Complexes. *Eur. J. Inorg. Chem.* **2001**, *2001*, 363–365. [[CrossRef](#)]
29. Costes, J.-P.; Shova, S.; Clemente-Juan, J.M.; Suet, N. The first example of a hetero-tetranuclear $[(\text{VO})\text{Gd}]_2$ complex: Synthesis, crystal structure and magnetic properties of $[\text{VO}(\text{Gd}(\text{hfa})_2\text{CH}_3\text{OH})_2 \cdot 2\text{CH}_3\text{OH} \cdot 2(\text{CH}_3)_2\text{CO}]$. *Dalton Trans.* **2005**, *17*, 2830–2832. [[CrossRef](#)]
30. Shi, W.; Chen, X.-Y.; Zhao, Y.-N.; Zhao, B.; Cheng, P.; Yu, A.; Song, H.-B.; Wang, H.-G.; Liao, D.-Z.; Yan, S.-P.; et al. Synthesis, Crystal Structures, and Properties of Oxovanadium(IV)–Lanthanide(III) Heteronuclear Complexes. *Chem. Eur. J.* **2005**, *11*, 5031–5039. [[CrossRef](#)]
31. Rocha, J.; Almeida Paz, F.A.; Shi, F.-N.; Ferreira, R.A.S.; Trindade, T.; Carlos, L.D. Photoluminescent Porous Modular Lanthanide–Vanadium–Organic Frameworks. *Eur. J. Inorg. Chem.* **2009**, *2009*, 4931–4945. [[CrossRef](#)]
32. Ishida, T.; Watanabe, R.; Fujiwara, K.; Okazawa, A.; Kojima, N.; Tanaka, G.; Yoshii, S.; Nojiri, H. Exchange coupling in TbCu and DyCu single-molecule magnets and related lanthanide and vanadium analogs. *Dalton Trans.* **2012**, *41*, 13609–13619. [[CrossRef](#)] [[PubMed](#)]
33. Hickson, J.R.; Horsewill, S.J.; Bamforth, C.; McGuire, J.; Wilson, C.; Sproules, S.; Farnaby, J.H. The modular synthesis of rare earth-transition metal heterobimetallic complexes utilizing a redox-active ligand. *Dalton Trans.* **2018**, *47*, 10692–10701. [[CrossRef](#)] [[PubMed](#)]
34. Das, D.; Guha, A.K. Supramolecular assembly of binuclear $[\text{V}_2\text{O}_3(\text{NTA})_2]^{4-}$ unit with $[\text{Ce}(\text{H}_2\text{O})_9]^{3+}$: Synthesis, structure, luminescent, magnetic properties and TD-DFT calculation. *Polyhedron* **2017**, *137*, 1–9. [[CrossRef](#)]
35. Shi, W.; Chen, X.-Y.; Zhao, B.; Yu, A.; Song, H.-B.; Cheng, P.; Wang, H.-G.; Liao, D.-Z.; Yan, S.-P. Construction of 3d-4f Mixed-Metal Complexes Based on a Binuclear Oxovanadium Unit: Synthesis, Crystal Structure, EPR, and Magnetic Properties. *Inorg. Chem.* **2006**, *45*, 3949–3957. [[CrossRef](#)]
36. Orendáč, M.; Sedláčková, L.; Čížmár, E.; Orendáčová, A.; Feher, A.; Zvyagin, S.A.; Wosnitza, J.; Zhu, W.H.; Wang, Z.M.; Gao, S. Spin relaxation and resonant phonon trapping in $[\text{Gd}_2(\text{fum})_3(\text{H}_2\text{O})_4]3\text{H}_2\text{O}$. *Phys. Rev.* **2010**, *B81*, 214410. [[CrossRef](#)]
37. Martínez-Pérez, M.J.; Cardona-Serra, S.; Schlegel, C.; Moro, F.; Alonso, P.J.; Prima-García, H.; Clemente-Juan, J.M.; Evangelisti, M.; Gaita-Ariño, A.; Sesé, J.; et al. Gd-Based Single-Ion Magnets with Tunable Magnetic Anisotropy: Molecular Design of Spin Qubits. *Phys. Rev. Lett.* **2012**, *108*, 247213. [[CrossRef](#)]
38. Rossin, A.; Giambastiani, G.; Peruzzini, M.; Sessoli, R. Amine-Templated Polymeric Lanthanide Formates: Synthesis, Characterization, and Applications in Luminescence and Magnetism. *Inorg. Chem.* **2012**, *51*, 6962–6968. [[CrossRef](#)] [[PubMed](#)]
39. Arauzo, A.; Lazarescu, A.; Shova, S.; Bartolomé, E.; Cases, R.; Luzón, J.; Bartolomé, J.; Turta, C. Structural and magnetic properties of some lanthanide ($\text{Ln} = \text{Eu}(\text{III})$, $\text{Gd}(\text{III})$ and $\text{Nd}(\text{III})$) cyanoacetate polymers: Field-induced slow magnetic relaxation in the Gd and Nd substitutions. *Dalton Trans.* **2014**, *43*, 12342–12356. [[CrossRef](#)]
40. Khalfaoui, O.; Beghidja, A.; Long, J.; Boussadia, A.; Beghidja, C.; Guari, Y.; Larionova, J. Cinnamic acid derivative rare-earth dinuclear complexes and one-dimensional architectures: Synthesis, characterization and magnetic properties. *Dalton Trans.* **2017**, *46*, 3943–3952. [[CrossRef](#)] [[PubMed](#)]
41. Girginova, P.I.; Pereira, L.C.J.; Coutinho, J.T.; Santos, I.C.; Almeida, M. Slow magnetic relaxation in lanthanide ladder type coordination polymers. *Dalton Trans.* **2014**, *43*, 1897–1905. [[CrossRef](#)]
42. Holmberg, R.J.; Ho, L.T.A.; Ungur, L.; Korobkov, I.; Chibotaru, L.F.; Murugesu, M. Observation of unusual slow-relaxation of the magnetisation in a Gd-EDTA chelate. *Dalton Trans.* **2015**, *44*, 20321–20325. [[CrossRef](#)] [[PubMed](#)]
43. Yoshida, T.; Cosquer, G.; Izuogu, D.C.; Ohtsu, H.; Kawano, M.; Lan, Y.; Wernsdorfer, W.; Nojiri, H.; Breedlove, B.K.; Yamashita, M. Field-Induced Slow Magnetic Relaxation of Gd^{III} Complex with a Pt–Gd Heterometallic Bond. *Chem. Eur. J.* **2017**, *23*, 4551–4556. [[CrossRef](#)]

44. Handzlik, G.; Magott, M.; Arczyński, M.; Sheveleva, A.M.; Tuna, F.; Sarewicz, M.; Osyczka, A.; Rams, M.; Vieru, V.; Chibotaru, L.F.; et al. Magnetization Dynamics and Coherent Spin Manipulation of a Propeller Gd(III) Complex with the Smallest Helicene Ligand. *J. Phys. Chem. Lett.* **2020**, *11*, 1508–1515. [[CrossRef](#)]
45. Bazhina, E.S.; Aleksandrov, G.G.; Kiskin, M.A.; Korlyukov, A.A.; Efimov, N.N.; Bogomyakov, A.S.; Starikova, A.A.; Mironov, V.S.; Ugolkova, E.A.; Minin, V.V.; et al. The First Series of Heterometallic Ln^{III}-V^{IV} Complexes Based on Substituted Malonic Acid Anions: Synthesis, Structure and Magnetic Properties. *Eur. J. Inorg. Chem.* **2018**, *2018*, 5075–5090. [[CrossRef](#)]
46. Llunell, M.; Casanova, D.; Cirera, J.; Alemany, P.; Alvarez, S. *SHAPE v.2.1, Program for the Stereochemical Analysis of Molecular Fragments by Means of Continuous Shape Measures and Associated Tools*; Universitat de Barcelona: Barcelona, Spain, 2013.
47. Casanova, D.; Llunell, M.; Alemany, P.; Alvarez, S. The Rich Stereochemistry of Eight-Vertex Polyhedra: A Continuous Shape Measures Study. *Chem. Eur. J.* **2005**, *11*, 1479–1494. [[CrossRef](#)] [[PubMed](#)]
48. Chilton, N.F.; Anderson, R.P.; Turner, L.D.; Soncini, A.; Murray, K.S. PHI: A powerful new program for the analysis of anisotropic monomeric and exchange-coupled polynuclear d- and f-block complexes. *J. Comput. Chem.* **2013**, *34*, 1164. [[CrossRef](#)]
49. Atzori, M.; Chiesa, A.; Morra, E.; Chiesa, M.; Sorace, L.; Carretta, S.; Sessoli, R. A two-qubit molecular architecture for electron-mediated nuclear quantum simulation. *Chem. Sci.* **2018**, *9*, 6183–6192. [[CrossRef](#)] [[PubMed](#)]
50. Atzori, M.; Tesi, L.; Benci, S.; Lunghi, A.; Righini, R.; Taschin, A.; Torre, R.; Sorace, L.; Sessoli, R. Spin Dynamics and Low Energy Vibrations: Insights from Vanadyl-Based Potential Molecular Qubits. *J. Am. Chem. Soc.* **2017**, *139*, 4338–4341. [[CrossRef](#)]
51. Atzori, M.; Morra, E.; Tesi, L.; Albino, A.; Chiesa, M.; Sorace, L.; Sessoli, R. Quantum Coherence Times Enhancement in Vanadium(IV)-based Potential Molecular Qubits: The Key Role of the Vanadyl Moiety. *J. Am. Chem. Soc.* **2016**, *138*, 11234–11244. [[CrossRef](#)]
52. Atzori, M.; Tesi, L.; Morra, E.; Chiesa, M.; Sorace, L.; Sessoli, R. Room-Temperature Quantum Coherence and Rabi Oscillations in Vanadyl Phthalocyanine: Toward Multifunctional Molecular Spin Qubits. *J. Am. Chem. Soc.* **2016**, *138*, 2154–2157. [[CrossRef](#)] [[PubMed](#)]
53. Atzori, M.; Benci, S.; Morra, E.; Tesi, L.; Chiesa, M.; Torre, R.; Sorace, L.; Sessoli, R. Structural Effects on the Spin Dynamics of Potential Molecular Qubit. *Inorg. Chem.* **2018**, *57*, 731–740. [[CrossRef](#)] [[PubMed](#)]
54. Tesi, L.; Lunghi, A.; Atzori, M.; Lucaccini, E.; Sorace, L.; Tottia, F.; Sessoli, R. Giant spin–phonon bottleneck effects in evaporable vanadyl-based molecules with long spin coherence. *Dalton Trans.* **2016**, *45*, 16635–16643. [[CrossRef](#)]
55. Kurganskii, I.V.; Bazhina, E.S.; Korlyukov, A.A.; Babeshkin, K.A.; Efimov, N.N.; Kiskin, M.A.; Veber, S.L.; Sidorov, A.A.; Eremenko, I.L.; Fedin, M.V. Mapping Magnetic Properties and Relaxation in Vanadium(IV) Complexes with Lanthanides by Electron Paramagnetic Resonance. *Molecules* **2019**, *24*, 4582. [[CrossRef](#)]
56. Katoh, K.; Yamashita, S.; Yasuda, N.; Kitagawa, Y.; Breedlove, B.K.; Nakazawa, Y.; Yamashita, M. Control of the Spin Dynamics of Single-Molecule Magnets by using a Quasi One-Dimensional Arrangement. *Angew. Chem. Int. Ed.* **2018**, *57*, 9262–9267. [[CrossRef](#)] [[PubMed](#)]
57. *SMART (Control) and SAINT (Integration) Software, Version 5.0*; Bruker AXS, Inc.: Madison, WI, USA, 1997.
58. Sheldrick, G.M. *SADABS, Program for Scaling and Correction of Area Detector Data*; Göttingen University: Göttingen, Germany, 1997.
59. Sheldrick, G.M. Crystal structure refinement with SHELXL. *Acta Crystallogr. Sect. A Found. Crystallogr.* **2015**, *71*, 3–8. [[CrossRef](#)]
60. Dolomanov, O.V.; Bourhis, L.J.; Gildea, R.J.; Howard, J.A.K.; Puschmann, H. OLEX2: A complete structure solution, refinement and analysis program. *J. Appl. Crystallogr.* **2009**, *42*, 339–341. [[CrossRef](#)]
61. Stoll, S.; Schweiger, A. EasySpin, a comprehensive software package for spectral simulation and analysis in EPR. *J. Magn. Reson.* **2006**, *178*, 42–55. [[CrossRef](#)]
62. Frisch, M.J.; Trucks, G.W.; Schlegel, H.B.; Scuseria, G.E.; Robb, M.A.; Cheeseman, J.R.; Scalmani, G.; Barone, V.; Mennucci, B.; Petersson, G.A.; et al. *Gaussian 09 (Revision E.01)*; Gaussian, Inc.: Wallingford, CT, USA, 2013.
63. Kohn, W.; Sham, L.J. Self-consistent equations including exchange and correlation effects. *Phys. Rev.* **1965**, *140*, A1133–A1138. [[CrossRef](#)]
64. Douglas, M.; Kroll, N.M. Quantum electrodynamical corrections to the fine structure of helium. *Ann. Phys.* **1974**, *82*, 89–155. [[CrossRef](#)]
65. Hess, B.A. Applicability of the no-pair equation with free-particle projection operators to atomic and molecular structure calculations. *Phys. Rev. A* **1985**, *32*, 756–763. [[CrossRef](#)] [[PubMed](#)]